technologies

MDPI

Article

Force–Depth–Stiffness Modeling of Rotary Ball-Burnished Dimples on an External Cylinder for Adaptive Guideway Stiffness Mapping

Kirill A. Bashmur *, Alexander V. Zagulyaev and Ivan S. Nekrasov

Department of Technological Machines and Equipment of Oil and Gas Complex, School of Petroleum and Natural Gas Engineering, Siberian Federal University, 660041 Krasnoyarsk, Russia
* Correspondence: bashmur@bk.ru

Abstract

This study develops a theoretical and computational mechanics framework for regular dimples produced by rotary ball burnishing on an external cylindrical surface. The model combines the local quadratic ball–cylinder gap, an effective mean indentation pressure H_{eff}, an unloading factor λ, residual dimple geometry, a Greenwood–Williamson pressure–approach law for the load-bearing lands, and an elastic spectral reference calculation. The dimple area fraction F_{n} is obtained from the periodic union of loaded-imprint footprints for the nominal stiffness maps, whereas the residual profile determines the specific oil capacity, defined as retained cavity volume per unit nominal area. Numerical checks include algebraic consistency, mesh-converged periodic FFT-BEM calculations, and a separate sinusoidal benchmark. For a representative 3 mm ball and 25 mm cylinder with $H_{\mathrm{eff}} = 2$ GPa, the model maps burnishing force and texture pitch to idle- and working-pressure secant stiffness. Within the stated range $F_{\mathrm{n}} \leq 0.20$, the low-fidelity index preserves the ordering of all evaluated non-tied design points; the mean and maximum differences from the spectral reference are 6.6% and 15.2%. A discrete force–pitch grid yields three feasible points under illustrative stiffness windows and two candidates after non-dominated sorting and secondary selection by specific oil capacity. The selected textures reduce idle-pressure stiffness slightly more than working-pressure stiffness, increasing the nonlinearity ratio from 5.70 to 5.91. The framework provides a reproducible model-based tool for preliminary force–pitch selection; application to a specific material–process pair requires identification of H_{eff}, λ, and the load-bearing-land response and validation against process-specific measurements.

Keywords: ball burnishing; external cylindrical surface; force–depth–stiffness model; regular microrelief; specific oil capacity; contact stiffness; contact compliance; dimples; adaptive stiffness; guideway

Check for updates

Academic Editor: Manoj Gupta

Received: 13 July 2026
Revised: 13 August 2026
Accepted: 17 August 2026
Published: 19 August 2026

Copyright: © 2026 by the authors. Licensee MDPI, Basel, Switzerland. This article is an open access article distributed under the terms and conditions of the Creative Commons Attribution (CC BY) license.

1. Introduction

Normal contact stiffness and contact compliance determine load transfer, local approach, vibration response, and positioning stability in assembled machine systems. In precision slideways and soft-guideway interfaces, the desired response combines high compliance at the idle pressure with a pronounced increase in contact stiffness toward the working pressure. Regular microrelief (RMR) is a periodic surface texture in which repeated depressions or grooves are separated by load-bearing lands. By redistributing the real contact area and local compliance, such a texture provides a passive means of tailoring

pressure-dependent response. The design objective is therefore a high ratio of working-pressure stiffness to idle-pressure stiffness while maintaining a prescribed working-stiffness floor. A manufacturing model for such surfaces must link process variables to the pressure–approach response rather than to a single roughness-height parameter alone [1–3].

In precision machine tools, load-dependent support has traditionally been achieved through hydrostatic or partially floated guideways, which require pumps, precision restrictors, and elaborate assembly [4,5]. Semi-active interfaces employing magnetorheological fluids can also tune contact stiffness, yet they depend on external magnetic fields and a continuous power supply [6]. Experimental investigations on sliding guideways with laser-textured micro-dimples have shown that passive textures can broaden the hydrodynamic lubrication region, reduce friction instability, and suppress stick–slip [7,8]. Rotary ball burnishing provides a chipless route for creating regular dimples by controlled plastic deformation. Because laser texturing and ball burnishing differ in dimple geometry, material modification, and process mechanics, the relationship between burnishing force and the resulting pressure-dependent normal contact stiffness remains insufficiently quantified for rotary ball-burnished external cylindrical surfaces.

Classical RMR studies and later rotary-body models establish the geometric basis by identifying relative area, pitch, overlap, and oil capacity as functional descriptors for hydraulic cylinders, slideways, and friction pairs [9–11]. Burnishing, vibroburnishing, ultrasonic-assisted burnishing, and thermomechanical treatments can create controlled textures by plastic deformation. Reviews and application studies relate force, feed, tool radius, groove dimensions, roughness, microhardness, and surface integrity to processing conditions [12–16].

Recent finite-element ball burnishing studies supported by experiments account for tool–surface friction, initial topography, strain hardening, residual-stress development, thermal history, and microstructural strengthening [17–22]. These studies demonstrate that residual geometry and surface integrity are material- and process-specific, but they generally target the forming stage rather than the subsequent pressure-dependent normal stiffness of a regular dimple array. The present framework complements these detailed forming simulations by providing a computationally efficient process-to-performance model for preliminary screening of the design space.

Beyond the forming stage, the functional performance of surface textures depends on dimple size, depth, density, debris storage, lubrication regime, and the real contact area of the lands between depressions [23–25]. Deterministic surface-shaping and vibromechanical texturing systems further show that prescribed tool motion can create micro-dimples and micro-grooves on cylindrical and flat surfaces [26,27]. On guideway specimens, micro-dimples have shifted the critical hydrodynamic point on the Stribeck curve, reduced stick–slip amplitude, and lowered friction relative to untextured guideways [7,8]. Regular textures have also been associated with changes in bearing dynamics and lubricant/debris retention [28,29]. Because burnished dimples are arranged regularly, their mesoscopic geometry is represented deterministically; the smaller-scale roughness of the intervening lands is represented statistically unless measured profilometry is available.

To translate the prescribed geometry into pressure-dependent stiffness, contact-mechanics models for rough and textured surfaces are required. The Greenwood–Williamson model, elastic–plastic asperity models, multiscale truncation, curved-surface stiffness formulations, and homogenized scale-coupled models provide pressure–approach relations [30–35]. Periodic contact analyses describe the interactions introduced by regular microgeometry [36,37], whereas FFT-based boundary-element studies provide numerical reference solutions from partial to near-complete contact [38,39].

The established forming and contact submodels do not by themselves provide a direct mapping from controllable burnishing force to residual depth, dimple area fraction, specific oil capacity, and pressure-dependent stiffness. Existing studies generally address either dimple formation without a service-stiffness map or regular-relief stiffness without a direct link to burnishing force. For an external cylindrical workpiece, a useful design procedure must therefore establish a force → depth → dimple geometry → stiffness/compliance chain and apply an explicit and reproducible selection rule to the force–pitch domain.

This work develops a direct force–depth–geometry–stiffness mapping for rotary ball burnishing of dimples on an external cylindrical surface. It first derives an explicit force-to-residual-depth relation from relative curvatures, an effective mean indentation pressure, and an unloading factor requiring process-specific identification. The resulting geometry is converted into periodic dimple area fraction, specific oil capacity, and a land pressure–approach response. Force–pitch stiffness maps are then evaluated under specified feasibility constraints, followed by non-dominated sorting and secondary selection based on specific oil capacity. An established land-fraction and pressure scaling is used as a low-fidelity screening index and is assessed against a spectral reference calculation through pointwise differences and rank preservation. The model is intended for shallow dimples in metallic substrates under quasi-static forming and room-temperature service conditions, and it provides preliminary process selection before material-specific identification, profilometry, or a full contact calculation. Accordingly, the contribution is a theoretical and computational mechanics framework for the force–depth–geometry–stiffness mapping.

2. Materials and Methods

2.1. Physical Basis of the Force–Depth Model

For a ball of radius R_b acting on a cylindrical workpiece of radius R_c, the principal relative curvatures in the axial and circumferential directions are

$$\kappa_{ax} = \frac{1}{R_b}, \qquad \kappa_{circ} = \frac{1}{R_b} + \frac{1}{R_c}. \tag{1}$$

In the tangent plane at the initial contact point, the undeformed local separation follows from the second-order expansion

$$g(x,y) = \frac{1}{2}\left(\kappa_{ax}x^2 + \kappa_{circ}y^2\right) + O(r^4), \qquad r^2 = x^2 + y^2.$$

The elliptic paraboloid is therefore the local quadratic representation of the ball–cylinder gap, not a global replacement of either surface [40]. At the maximum force considered, the largest loaded semi-axis is 0.260 mm, giving $a_{max}/R_b = 0.087$ and $a_{max}/R_c = 0.010$; the contact region consequently remains small relative to both radii.

Denoting the quadratic term above by $g_2(x,y)$, the exact external ball–cylinder separation in the same tangent coordinates is

$$g_{exact}(x,y) = R_b - \sqrt{R_b^2 - x^2 - y^2} + R_c - \sqrt{R_c^2 - y^2}.$$

For the largest loaded footprint ($F_N = 400$ N), $a_{ax} = 0.260$ mm and $a_{circ} = 0.245$ mm. The remainder $e_g = g_{exact} - g_2$ reaches its maximum at the axial edge, where $e_g = 0.021$ µm, or 0.19% of the quadratic boundary gap; at the circumferential edge it is 0.017 µm. This supports the adequacy of the second-order local-gap representation over the investigated geometric domain.

For the reference calculation, $R_b = 3$ mm, $R_c = 25$ mm, $E = 210$ GPa, and $\nu = 0.30$. The baseline $H_{eff} = 2$ GPa corresponds numerically to approximately 204 HV. It is used

here as an effective mean indentation pressure rather than as a measured hardness of a specific steel; material-specific application requires identification from force–depth or residual-profile data. Assuming that the mean pressure over the projected plastic imprint is H_{eff}, force balance gives $F_{\mathrm{N}} = H_{\mathrm{eff}} A_{\mathrm{proj}}$, where $A_{\mathrm{proj}} = \pi a_{\mathrm{ax}} a_{\mathrm{circ}}$ and $a_i = \sqrt{2h_{\mathrm{ind}}/\kappa_i}$. Consistent with the classical interpretation of hardness as a mean indentation pressure [40,41],

$$h_{\mathrm{ind}} = \frac{F_{\mathrm{N}} \sqrt{\kappa_{\mathrm{ax}} \kappa_{\mathrm{circ}}}}{2\pi H_{\mathrm{eff}}}. \tag{2}$$

The elastic unloading displacement is represented by

$$h_{\mathrm{rec}} = \lambda \frac{F_{\mathrm{N}}}{2E^* a_{\mathrm{eq}}}, \qquad E^* = \frac{E}{1-\nu^2}, \qquad a_{\mathrm{eq}} = \sqrt{a_{\mathrm{ax}} a_{\mathrm{circ}}}, \tag{3}$$

where λ is an effective unloading factor. The reference value $\lambda = 1$ corresponds to the displacement of an area-equivalent circular flat punch in Equation (3), following standard indentation-unloading concepts. Both H_{eff} and λ must be identified for the target material–process pair. The residual dimple depth after unloading is

$$h_{\mathrm{res}} = \max(0, h_{\mathrm{ind}} - h_{\mathrm{rec}}). \tag{4}$$

The variables h_{ind}, h_{res}, and $\delta(q)$ describe different physical quantities: indentation depth under the forming force, residual dimple depth after unloading, and normal approach of the textured interface under nominal pressure.

The calculation sequence combines established submodels for mean indentation pressure [41], nonconforming contact and equivalent-punch unloading [40,42], Greenwood–Williamson land contact [30], and the elastic half-space Green function [38,39]. Their integration into the force → depth → geometry → stiffness sequence requires material–process-specific identification of H_{eff} and λ. Figure 1 summarizes the structure.

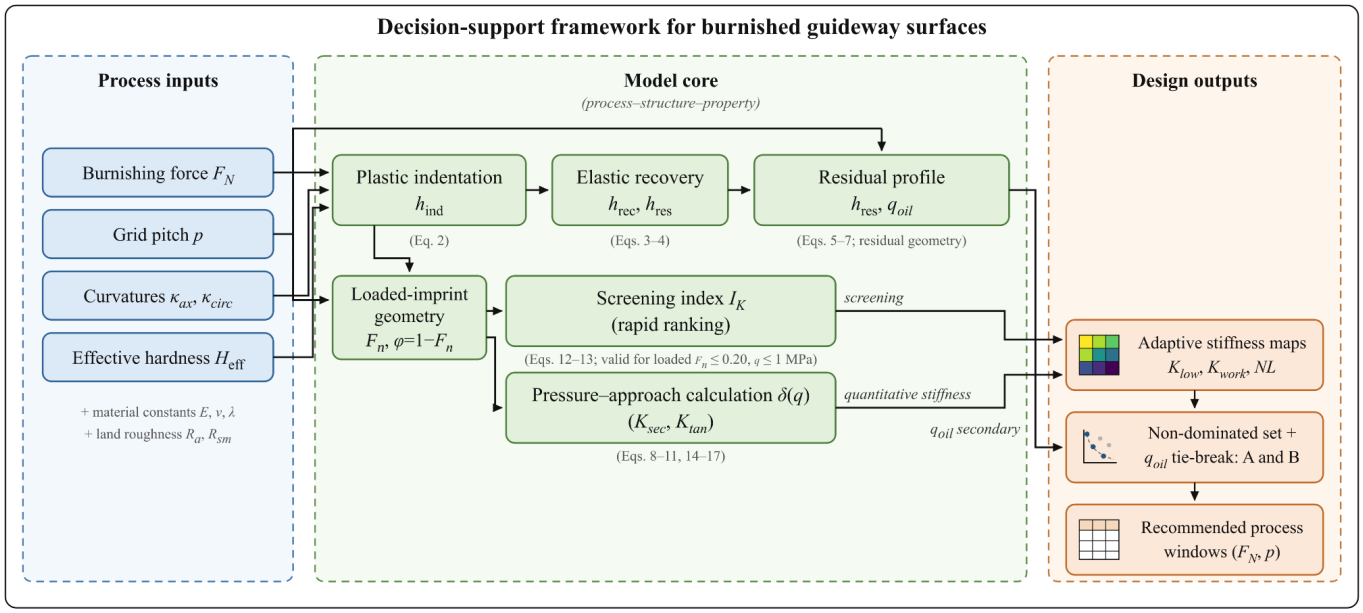


Figure 1. Architecture of the proposed decision-support framework for burnished guideway surfaces. Process inputs are transformed through the force–depth, elastic-recovery, residual-geometry, screening-index, and pressure–approach modules into adaptive stiffness maps, non-dominated candidates, and illustrative candidate process windows. The framework applies to metallic substrates under quasi-static forming and room-temperature service conditions.

2.2. Dimple Geometry and Functional Metrics

The spherical-unloading approximation defines the residual geometry in the force sweep, whereas the curvature-based residual-profile approximation provides the alternative geometry used in the sensitivity analysis. Let

$$r_{\mathrm{ind}} = \sqrt{2R_{\mathrm{b}}h_{\mathrm{ind}}}, \qquad r_{\mathrm{res},0} = \sqrt{2R_{\mathrm{b}}h_{\mathrm{res}}}$$

be the shallow spherical-cap radii associated with the loaded indentation depth and the residual depth if the tool curvature is retained. The force-sweep footprint radius is approximated as their geometric mean, $r_{\mathrm{sph}} = \sqrt{r_{\mathrm{ind}}r_{\mathrm{res},0}}$, giving

$$A_{\mathrm{sph}} = \pi r_{\mathrm{sph}}^2 = 2\pi R_{\mathrm{b}}\sqrt{h_{\mathrm{ind}}h_{\mathrm{res}}}, \qquad V_{\mathrm{sph}} = \frac{1}{2}A_{\mathrm{sph}}h_{\mathrm{res}}.$$

For shallow indentations, the geometric-mean radius ensures that the reconstructed residual footprint vanishes continuously as $h_{\mathrm{res}} \to 0$. The spherical-unloading approximation is used for the force sweep because shallow rigid-sphere indentation tends to inherit the tool curvature when pile-up and sink-in are limited; the assumptions and calibration limits follow the classical indentation discussion of Tabor and Johnson [40,41].

The curvature-based residual-profile approximation is evaluated separately to quantify sensitivity to the assumed post-unloading geometry. It reconstructs an elliptic paraboloid solely from the residual depth and the relative curvatures of the cylindrical workpiece, with semi-axes

$$a_i = \sqrt{\frac{2h_{\mathrm{res}}}{\kappa_i}}, \qquad i \in \{\mathrm{ax}, \mathrm{circ}\}. \tag{5}$$

The curvature-based reconstruction is used only for sensitivity analysis. For this approximation and for the periodic design-map depth fields, the local cavity volume associated with one elliptic-parabolic footprint is

$$V = \frac{1}{2}\pi a_{\mathrm{ax}}a_{\mathrm{circ}}h_{\mathrm{res}}. \tag{6}$$

For a periodic cell of area A_{cell}, the dimple area fraction and the overlap-corrected specific oil capacity are

$$F_{\mathrm{n}} = \frac{A_{\mathrm{union}}}{A_{\mathrm{cell}}}, \qquad q_{\mathrm{oil}} = \frac{V_{\mathrm{union}}}{A_{\mathrm{cell}}}. \tag{7}$$

Both quantities are evaluated from the same periodic union. If $\rho_j^2 = [(x - x_j)/a_{\mathrm{ax}}]^2 + [(y - y_j)/a_{\mathrm{circ}}]^2$ for replica j, then the periodic-union cavity volume is

$$V_{\mathrm{union}} = \int_{A_{\mathrm{cell}}} \max_j \left[h_{\mathrm{res}} \max(0, 1 - \rho_j^2)\right] \mathrm{d}A,$$

whereas A_{union} is the area on which the maximum depth is positive. The periodic union was evaluated numerically; the replica extent, integration grid, and grid-refinement checks are reported in Supplementary Section S1. The isolated-dimple sum V/A_{cell} is reported only as an upper bound and is excluded from design selection. In the reference parameter sweep, $A_{\mathrm{cell}} = 1.113\ \mathrm{mm}^2$, corresponding to rounded cell sides of 1.055 mm × 1.055 mm.

For the nominal stiffness maps, the land fraction is computed from the periodic union of the loaded-imprint footprints, whose semi-axes are $a_i^{\mathrm{load}} = \sqrt{2h_{\mathrm{ind}}/\kappa_i}$. Within the adopted monotonic land-stiffness closure, the loaded-imprint union is used as a conservative nominal geometry because it leaves less load-bearing land and therefore gives lower stiffness than the residual-depth reconstruction.

Across 200–400 N, the spherical-unloading residual footprint is 12–20% smaller than the loaded imprint, showing how elastic recovery changes the land fraction inferred from the post-unloading geometry.

The post-unloading profile determines residual depth and specific oil capacity and is examined separately in Section 3.6. Figure 2 defines the cylindrical-workpiece geometry and projected semi-axes.

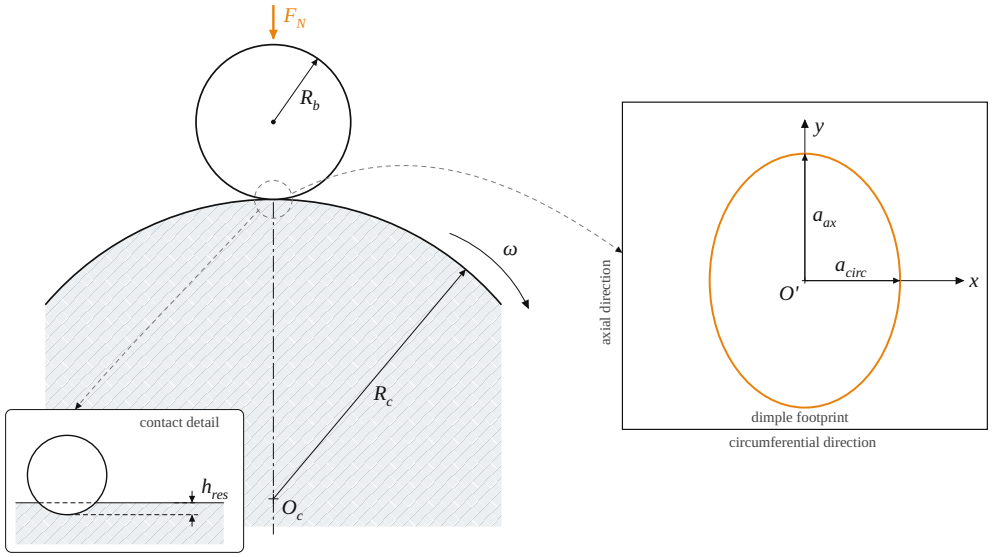


Figure 2. Cylindrical-workpiece burnishing geometry. The ball radius is R_b, the workpiece radius is R_c, h_{res} is the residual depth, and a_{ax} and a_{circ} are the projected semi-axes on the unwrapped surface.

2.3. Pressure–Approach Model and Stiffness Definitions

The deterministic dimple array removes a fraction F_n of the nominal area from the initial load-bearing land. The land fraction is

$$\phi = 1 - F_n, \tag{8}$$

and the mean pressure acting on the land is $q_{land} = q_{nom}/\phi$. The general pressure–approach relation separates the land roughness contribution from the deterministic dimple contribution,

$$\delta(q) = \delta_{land}\left(\frac{q}{\phi}\right) + \delta_{reg}(q). \tag{9}$$

The land term can be supplied by a measured pressure–approach curve or by a roughness model. In the present study it is evaluated using a Greenwood–Williamson contact model,

$$q_{land} = \eta_s \frac{4}{3} E^* R_s^{1/2} \int_d^\infty (z-d)^{3/2} f_z(z)\, dz, \tag{10}$$

with the generalized-Gaussian summit distribution

$$f_z(z) = \frac{\beta}{2\alpha_\beta \sigma \Gamma(1/\beta)} \exp\left[-\left(\frac{|z|}{\alpha_\beta \sigma}\right)^\beta\right], \qquad \alpha_\beta = \sqrt{\frac{\Gamma(1/\beta)}{\Gamma(3/\beta)}}, \qquad \beta = 2.30.$$

The profile descriptors are converted by $\sigma = \sqrt{\pi/2}\, R_a$, $R_s = R_{sm}^2/(4\pi^2\sigma)$, and $\eta_s = C_\eta / R_{sm}^2$. The numerical quadrature, profile-to-summit coefficients, pressure grid, and reproduction points are reported in Supplementary Section S1. The land approach is $\delta_{land} = 10^3(d_0 - d)$ in micrometers and the integral is inverted for d at each land pressure.

The plasticity indicator is $\chi_{GW} = (E^*/H_s)\sqrt{\sigma/R_s}$. The local summit hardness H_s is used only to screen the applicability of the elastic summit formulation and does not enter Equation (10). The adopted value $H_s = 6$ GPa is an illustrative value for a hardened steel land and lies below the reported nanohardness range of 8.61–17.03 GPa for microindented 100Cr6 steel [43]. It differs from H_{eff}: H_{eff} is the tool-scale effective mean pressure used in the burnishing force–area relation, whereas H_s characterizes microscopic land summits. Parameter sets with $\chi_{GW} \leq 0.30$ are evaluated with the elastic formulation; larger values fall outside its screening range and should be treated with an elastic–plastic land model.

The roughness and material sensitivity analysis uses a fixed reference cell with $F_n = 0.20$ and $\phi = 0.80$. For this sweep and for the nominal design maps, each nominal pressure is supplied to Equation (10) as $q_{land} = q_{nom}/\phi$. The reported map stiffness is therefore

$$K_{sec}(q_{nom}) = \frac{q_{nom}}{\delta_{land}(q_{nom}/\phi)}.$$

For the nominal maps, $\delta_{reg} = 0$ defines the land-only screening closure; its candidate-specific magnitude is quantified in Section 3.4 and Supplementary Section S1.6. The deterministic spectral term in Equations (14)–(17) is calculated separately to assess the screening index and is not included in K_{low} or K_{work}. A measured land curve may replace Equation (10) without changing the geometric or selection modules.

The secant and tangent stiffnesses are defined as

$$K_{sec}(q) = \frac{q}{\delta(q)}, \qquad K_{tan}(q) = \left(\frac{d\delta}{dq}\right)^{-1}. \tag{11}$$

Compliance is reported as $\delta(q)/q$ or $1/K$. The residual depth h_{res} defines the cavity height field and is distinct from the interfacial approach $\delta(q)$.

2.4. Screening Index and Spectral Reference Method

For preliminary screening, the low-fidelity index is used to rank the design points through a dimensionless land-area and pressure scaling,

$$I_K = \Phi_A(\phi)\,\Phi_q(q), \qquad \Phi_A = \phi^{m_K}, \qquad \Phi_q = \left(1 + \frac{q}{q_0}\right)^{-1}. \tag{12}$$

For shallow dimples with a positive load-bearing land, the first-order area factor is $\Phi_A = A_{land}/A_0 = \phi$ and $m_K = 1$. The [0/1] Padé pressure factor gives a monotonic ranking relation. With $q_0 = 1$ MPa,

$$I_K = \frac{\phi}{1 + q/(1\ \text{MPa})}. \tag{13}$$

The index is applied over $0 \leq q \leq 1$ MPa, $F_n \leq 0.20$, shallow residual depths, and positive land fraction. Quantitative stiffness is obtained from the pressure–approach calculation. Design points whose index separation is comparable to the quantified index–spectral discrepancy, or that lie near a decision boundary, are re-evaluated with the full spectral calculation.

The spectral reference calculation is based on Green's function for normal displacement of an elastic half-space, as used in FFT-based contact calculations and wavy-surface analyses [37–39]. For a periodic pressure field in a rectangular cell with periods p_x and p_y, the nonzero Fourier components satisfy

$$\hat{u}(\mathbf{k}_{mn}) = \frac{2}{E^*|\mathbf{k}_{mn}|}\hat{p}(\mathbf{k}_{mn}), \qquad \mathbf{k}_{mn} = \left(\frac{2\pi m}{p_x}, \frac{2\pi n}{p_y}\right), \quad (m,n) \neq (0,0). \tag{14}$$

The dimensionless field $g(x, y)$ represents the zero-mean residual cavity depth normalized by the fixed height $h_g = 1$ µm rather than binary cavity occupancy. The continuous Fourier coefficients are defined as

$$\widehat{g}_{mn} = \frac{1}{p_x p_y} \int_0^{p_x} \int_0^{p_y} g(x, y) \exp(-i\mathbf{k}_{mn} \cdot \mathbf{x}) \, \mathrm{d}y \, \mathrm{d}x. \tag{15}$$

Numerically, g is sampled at cell-centered points on an $N \times N$ grid and the coefficients are normalized as $\widehat{g}_{mn} = \mathrm{FFT}(g)_{mn}/N^2$. The deterministic contribution is summarized by the energy-equivalent compliance length

$$\Lambda_{\mathrm{spec}} = 2 \sum_{(m,n)\neq(0,0)} \frac{|\widehat{g}_{mn}|^2}{|\mathbf{k}_{mn}|} W(|\mathbf{k}_{mn}|L), \qquad W(\xi) = \frac{\tanh \xi}{\xi}, \tag{16}$$

Here, Λ_{spec} represents the additional compliance length that would produce the same elastic strain energy as the actual dimple field under a unit pressure. The gauge length is $L = \min(p_x, p_y)/2$. The factor W is a finite-gauge regularization: it approaches unity as $\xi \to 0$ and decays as $1/\xi$ at high wavenumber, attenuating contributions with wavelengths shorter than the chosen gauge length. The $(0, 0)$ mode is excluded because the mean land approach is already represented by Equation (10). The corresponding linear compliance increment is

$$\delta_{\mathrm{reg}}(q) = 10^3 \frac{q}{E^*} \Lambda_{\mathrm{spec}}, \tag{17}$$

with q and E^* in MPa, Λ_{spec} in mm, and δ_{reg} in micrometers. The spectral reference was evaluated on a converged periodic grid; the resolution and grid-refinement results are reported in Supplementary Section S1. Because this linear spectral sum does not impose unilateral contact/non-contact constraints, it is used only to normalize and assess the screening index. Those constraints are imposed separately in the FFT-BEM check.

For the FFT-BEM calculation, the residual height map is placed in a periodic square cell of area 1.113 mm^2 (rounded side length 1.055 mm) and loaded to a prescribed mean pressure of 1 MPa. The non-adhesive periodic contact problem was solved with a projected-gradient FFT-BEM method. Mesh-refinement data, the sinusoidal benchmark, and residual tolerances are reported in Supplementary Section S1.

2.5. Adaptive Stiffness-Map Design Case

Here, a "soft guideway" denotes an interface with low secant stiffness at the idle pressure and a pronounced stiffness increase toward the working pressure. In this work, "adaptive" refers to the passive pressure-dependent increase in secant stiffness, not to active control or absolute stiffening relative to an untextured reference. The comparison with the nearly untextured reference is therefore based on the nonlinearity ratio together with the absolute working-stiffness floor. The analysis uses $q_{\mathrm{idle}} = 0.10$ MPa, $q_{\mathrm{work}} = 1.00$ MPa, and $q_{\mathrm{high}} = 5.00$ MPa. The idle- and working-pressure metrics are

$$K_{\mathrm{low}} = K_{\mathrm{sec}}(q_{\mathrm{idle}}), \qquad K_{\mathrm{work}} = K_{\mathrm{sec}}(q_{\mathrm{work}}), \qquad NL = \frac{K_{\mathrm{work}}}{K_{\mathrm{low}}}. \tag{18}$$

The illustrative windows are $K_{\mathrm{low}} < 0.22$ and $K_{\mathrm{work}} > 1.20$ MPa/µm. The first promotes low-pressure compliance, whereas the second is a minimum working-stiffness floor. These thresholds define an illustrative design case for the selection procedure; application-specific limits must be derived from allowable carriage deflection, frictional restraint, guideway load distribution, and positioning error.

2.6. Assumptions and Validity Range

The model applies to shallow residual dimples in metallic substrates under quasi-static forming and room-temperature service conditions. The dimple bottoms remain out of contact over the considered pressure range, the tool is treated as rigid relative to the affected near-surface layer, and the local contact semi-axes remain much smaller than the tool and workpiece radii. The spherical-unloading approximation requires $h_{res}/R_b \ll 1$ and no dominant pile-up or sink-in; measured profilometry replaces the analytical profile when these conditions are not met. If the footprint becomes comparable with the texture pitch, the periodic union remains geometrically defined, but a unilateral periodic contact calculation is required for quantitative stiffness.

3. Results

3.1. Force Sweep and Residual Dimple Geometry

Across 20–400 N, indentation depth, residual depth, dimple area fraction, and specific oil capacity all increase with forming force (Figure 3). Residual dimples appear when elastic recovery no longer closes the loaded indentation. At $F_N = 100$ N, the model gives $h_{ind} = 2.81$ µm, $h_{rec} = 1.72$ µm, and $h_{res} = 1.09$ µm (Table 1).

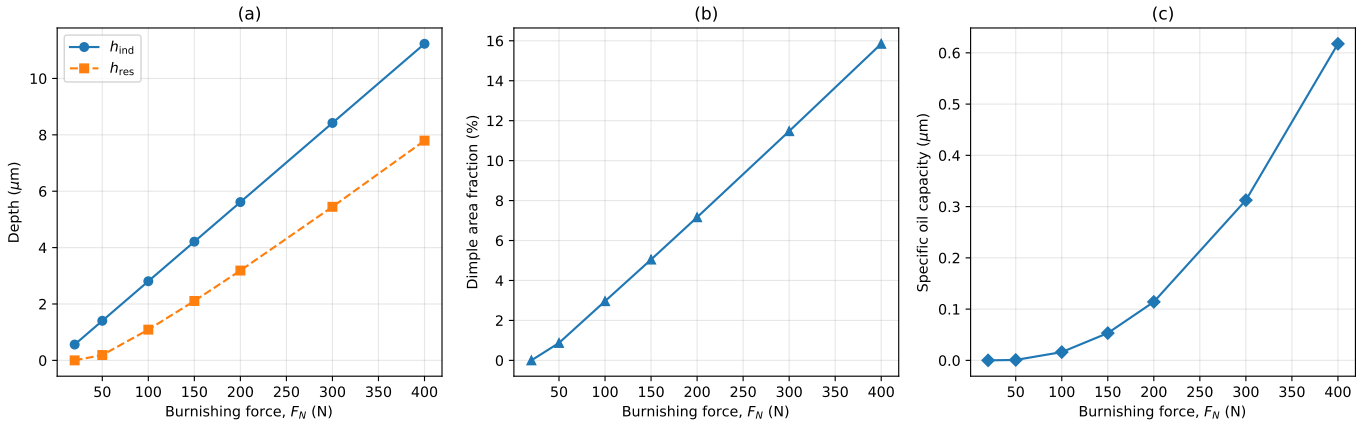


Figure 3. Force-to-depth, dimple-area-fraction, and specific-oil-capacity response for the spherical-unloading approximation: (**a**) indentation and residual depths versus normal force; (**b**) dimple area fraction; (**c**) specific oil capacity.

Table 1. Selected outputs for the spherical-unloading approximation.

F_N (N)	h_{ind} (µm)	h_{res} (µm)	F_n (%)	q_{oil} (µm)
50	1.40	0.19	0.9	0.0008
100	2.81	1.09	3.0	0.016
150	4.21	2.11	5.0	0.053
200	5.61	3.19	7.2	0.114
300	8.42	5.45	11.5	0.313
400	11.23	7.79	15.8	0.618

Elastic recovery accounts for a substantial fraction of the loaded indentation, especially at low forming force (Figure 4). At higher force, the residual depth increases more rapidly in relative terms than the dimple area fraction, and the retained volume increases rapidly.

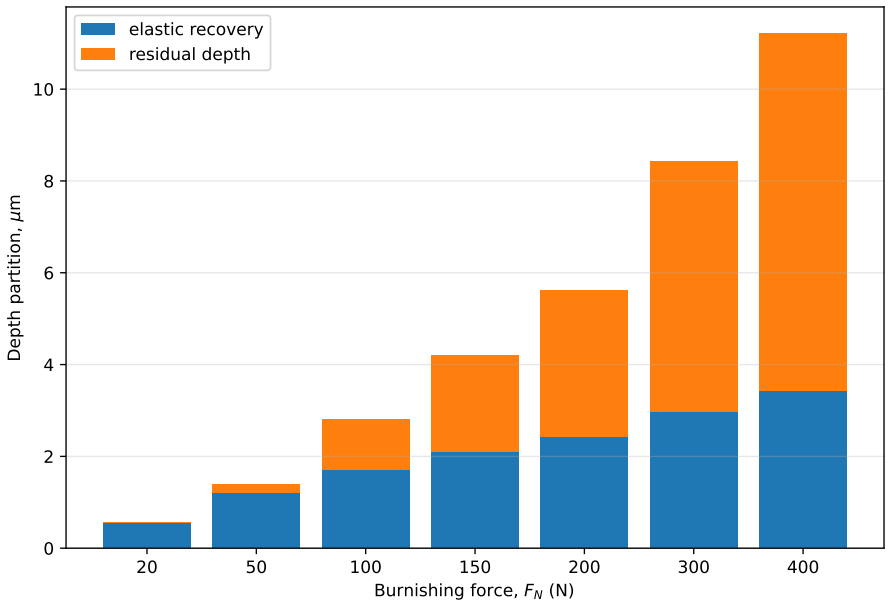


Figure 4. Loaded depth, elastic recovery and residual depth as functions of normal force.

3.2. Comparison of Residual-Profile Approximations

The curvature-based residual-profile approximation and the spherical-unloading approximation use the same force and recovered depth but reconstruct the residual footprint differently. At 100 N, the curvature-based residual area is approximately 41% below the spherical-unloading value. This area difference indicates substantial sensitivity to the assumed residual-profile reconstruction (Figure 5).

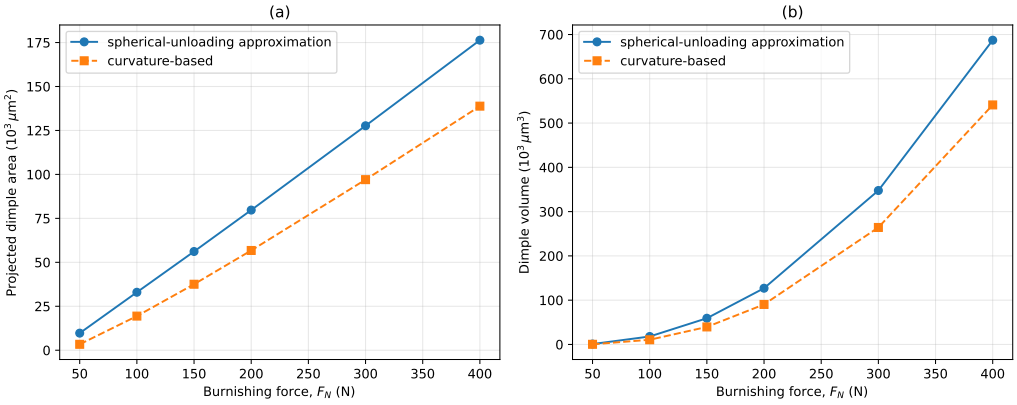


Figure 5. Projected dimple area and volume from the spherical-unloading approximation and the curvature-based residual-profile approximation: (**a**) projected dimple area and (**b**) dimple volume versus normal force.

Table 2 compares the two residual-profile approximations at 200 and 400 N. At 200 N, the curvature-based approximation lowers both residual area and isolated-cavity volume by 28.8%; at 400 N, the difference is 21.3%.

Table 2. Residual geometry calculated with the spherical-unloading and curvature-based residual-profile approximations. Areas and volumes are isolated-dimple values before periodic clipping.

F_N (N)	h_{res} (µm)	A_{sph} (10^3 µm^2)	A_{curv} (10^3 µm^2)	ΔA (%)	V_{sph} (10^3 µm^3)	V_{curv} (10^3 µm^3)	ΔV (%)
200	3.19	79.7	56.7	−28.8	127.0	90.4	−28.8
400	7.79	176.3	138.8	−21.3	687.2	541.0	−21.3

The decreasing relative discrepancy is specific to the adopted unloading approximation. At low force, elastic recovery removes most of the loaded indentation, so reconstructing the footprint solely from h_{res} produces a substantially smaller curvature-based footprint. As force increases, the retained-to-loaded depth ratio rises and the curvature-based reconstruction approaches the tool-inherited spherical footprint. The difference therefore arises from the assumed retention of tool curvature during unloading, not from a change in material properties.

3.3. Parameter Sensitivity

The first-order sensitivity of the loaded indentation depth follows from Equation (2):

$$\frac{dh_{ind}}{h_{ind}} = \frac{dF_N}{F_N} - \frac{dH_{eff}}{H_{eff}} + \frac{1}{2}\left(\frac{d\kappa_{ax}}{\kappa_{ax}} + \frac{d\kappa_{circ}}{\kappa_{circ}}\right). \tag{19}$$

A 5% change in H_{eff} therefore produces a 5% change in h_{ind}, whereas the same relative change in either curvature contributes half as much to the relative change in h_{ind} when the other curvature is fixed. Residual depth is more sensitive because it is the difference between loaded indentation and elastic recovery. Table 3 quantifies the effect of λ at three representative forces.

Table 3. Residual depth h_{res} for the unloading-factor sensitivity calculation. Candidate A and Candidate B correspond to 200 and 400 N, respectively.

Case	F_N (N)	$\lambda = 0.8$	$\lambda = 1.0$ h_{res} (μm)	$\lambda = 1.2$
Reference force	100	1.43	1.09	0.75
Candidate A	200	3.67	3.19	2.70
Candidate B	400	8.48	7.79	7.11

At the candidate forces, h_{res} remains positive throughout $\lambda = 0.8$–1.2. The stiffness-based selection is unchanged because the nominal maps use the loaded-imprint land fraction, so K_{low}, K_{work}, and feasibility do not depend on λ in those maps. Changing λ affects residual geometry and specific oil capacity; direct periodic volume calculations with the same clipping rule preserve the Candidate B–Candidate A oil-capacity ordering over this range. At 50 N, $\lambda = 1.2$ closes the residual dimple, showing that λ must be identified from measured residual profiles in the shallow-dimple regime.

3.4. Numerical Verification

The projected plastic area was checked against F_N/H_{eff} and found to match within numerical precision, confirming the algebraic consistency of Equation (2). Periodic FFT-BEM calculations were then used to assess how contact-area fraction changes with residual cavity depth at a fixed mean pressure. The resulting contact-area fractions and force-derived depths are reported in Table 4 and Figure 6.

Table 4. FFT-BEM contact-area verification points for the cylindrical-workpiece dimple cell at $p_{ref} = 1$ MPa.

F_N (N)	h_{ind} (μm)	h_{res} (μm)	Contact Area Fraction
50	1.40	0.19	0.991
100	2.81	1.09	0.970
150	4.21	2.11	0.950
200	5.61	3.19	0.928

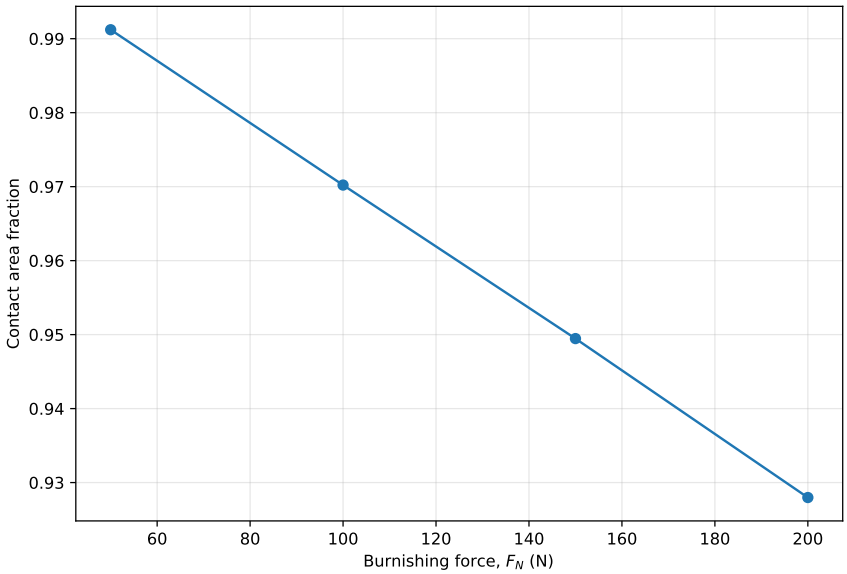


Figure 6. Periodic FFT-BEM contact-area fractions for the fixed cylindrical-workpiece cell at $q = 1$ MPa.

Mesh refinement changes the 200 N contact-area fraction by less than 0.1% between the 64^2 and 128^2 meshes. The separate sinusoidal benchmark differs from the Westergaard contact fraction by 3.0% on the final mesh, and the load and complementarity residuals satisfy the prescribed tolerances (Supplementary Section S1).

The screening index in Equation (13) was compared with the spectral reference calculation for the force–pitch grid at $q = 1$ MPa. Both quantities were normalized by the lightly textured baseline $F_N = 20$ N, $p = 1000\,\mu$m. Over the stated applicability range ($F_n \leq 0.20$, 14 grid points), the index preserves the spectral ranking exactly: Spearman $\rho = 1.00$, Kendall $\tau = 1.00$, and zero pairwise inversions occur among the 89 non-tied pairs. The two tied pairs arise from grid points with identical land fraction and are differentiated by specific oil capacity. The mean relative difference is 6.6% and the maximum is 15.2% (Figure 7; Table 5).

The pointwise relative differences remain below 10% for $F_n \leq 0.10$ and reach approximately 15% at $F_n \approx 0.20$ (Figure 8). Candidates whose index values differ by no more than the local discrepancy level are treated as tied and differentiated by specific oil capacity; points near a decision boundary are re-evaluated with the full spectral calculation.

Table 5. Screening index versus the spectral reference calculation at $q = 1$ MPa for all 14 grid points with $F_n \leq 0.20$. Values are normalized by the 20 N, 1000 µm baseline.

F_N (N)	p (µm)	F_n	$I_K/I_{K,0}$	$K_{spec}/K_{spec,0}$	Difference (%)
20	250	0.160	0.849	0.963	11.9
20	350	0.082	0.928	0.983	5.7
20	500	0.040	0.970	0.993	2.4
20	750	0.018	0.992	0.998	0.6
20	1000	0.010	1.000	1.000	0.0
50	500	0.100	0.909	0.979	7.1
50	750	0.044	0.965	0.992	2.7
50	1000	0.025	0.985	0.997	1.2
100	500	0.200	0.808	0.953	15.2
100	750	0.089	0.920	0.981	6.2
100	1000	0.050	0.960	0.991	3.2
200	750	0.178	0.831	0.959	13.4
200	1000	0.100	0.909	0.979	7.1
400	1000	0.200	0.808	0.953	15.2

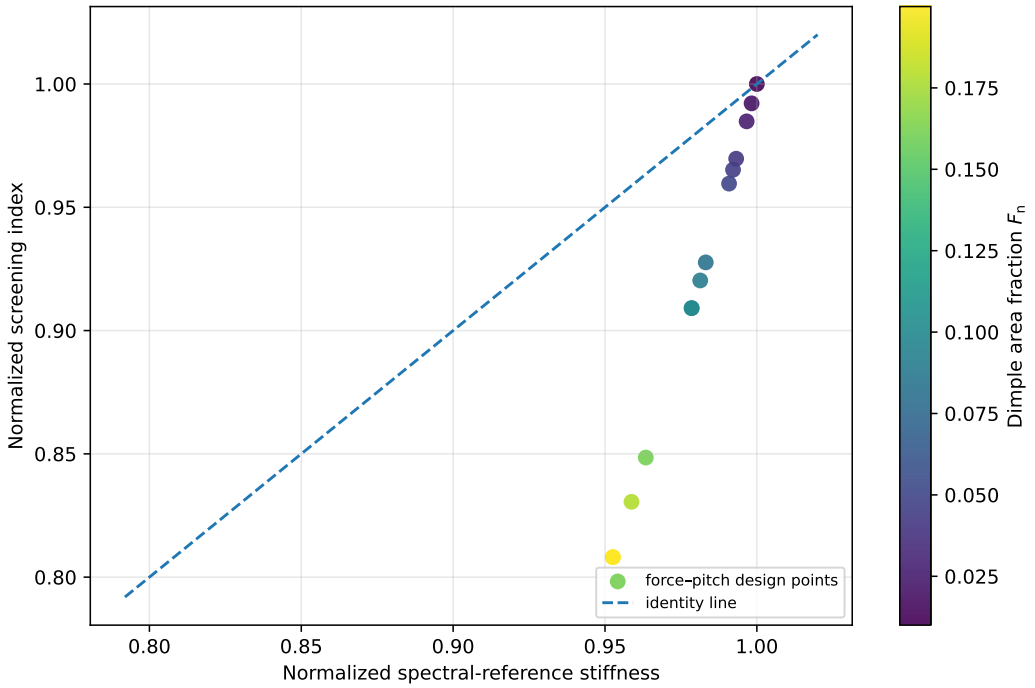


Figure 7. Comparison of the normalized screening index with the normalized spectral-reference stiffness at $q = 1$ MPa for the applicability range $F_n \leq 0.20$.

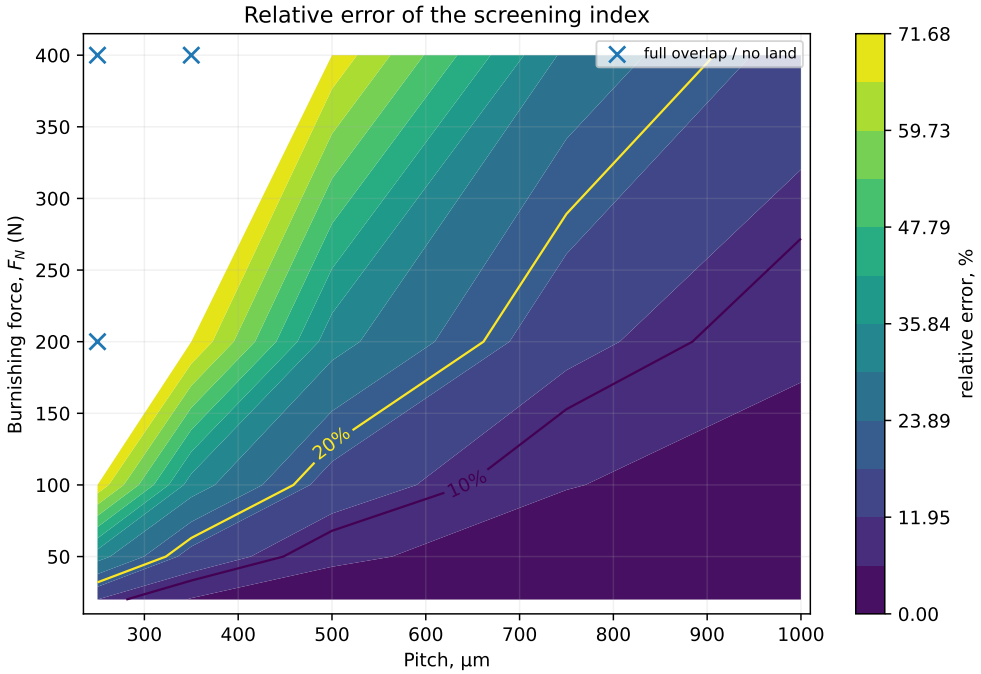


Figure 8. Pointwise relative difference between the normalized screening index and the normalized spectral-reference stiffness over the force–pitch grid. The contours show 10% and 20% difference levels; points near a screening boundary or separated by a comparable index difference are re-evaluated with the full spectral calculation. Crosses denote full-overlap points with $F_n = 1$; because no load-bearing land remains, the screening index is not applicable at these points.

Approximation, Residual, and Error Analysis

Table 6 separates numerical and analytical error measures from model-form and parameter sensitivities.

Table 6. Consolidated numerical-error and model-uncertainty budget. Values in the main text are rounded to physically meaningful precision; the entries represent distinct sources of numerical error, approximation error, and model uncertainty.

Category	Check	Maximum Magnitude	Interpretation
Geometric truncation	Exact gap versus quadratic gap	0.021 μm (0.19%)	Local second-order gap error over the largest investigated footprint.
GW reproduction	Direct quadrature check	0.6%	Numerical reproduction of the implemented land law.
Discretization	Periodic volume, spectral, and FFT-BEM meshes	Relative change in $q_{oil} < 0.001\%$; relative change in $\Lambda_{spec} < 0.001\%$; contact-fraction change $< 0.1\%$	Grid sensitivity of the corresponding calculations.
Solver and benchmark	Load/gap/complementarity residuals; sinusoidal reference	Load error $< 1.2 \times 10^{-16}$; maximum negative gap $< 3 \times 10^{-11}$ mm; complementarity residual $< 1.5 \times 10^{-8}$; sinusoidal-benchmark difference 3.0%	Algorithmic convergence and an elastic implementation check.
Omitted spectral term	Restore δ_{reg} for Candidates A and B	<0.2% change in K_{sec}	Magnitude diagnostic for the term omitted from the nominal land-only maps.
Screening approximation	Low-fidelity index versus spectral reference	Mean 6.6%; maximum 15.2%	Model discrepancy for ranking, not a solver error.
Residual-profile model form	Loaded-imprint versus curvature-based reconstruction	21–29% in residual area; 19–28% in candidate stiffness	Largest examined model-form sensitivity; the feasible set changes.
Material and surface parameters	H_{eff}, λ, E, and land roughness	Ranges reported in Sections 3.3 and 3.7	Parameter uncertainty requiring material–process identification.

The geometric, quadrature, grid, solver, and omitted-term effects are small relative to the post-unloading profile sensitivity. Restoring δ_{reg} changes the candidate secant stiffnesses by at most about 0.17%; the corresponding rounded bound is less than 0.2%. By contrast, residual-profile reconstruction changes candidate stiffness and feasibility. The H_{eff}, λ, elastic-modulus, and land-roughness variations are therefore treated as separate uncertainty sources.

These checks bound the numerical and analytical error of the implemented model; quantitative transfer remains governed by residual-profile, material-response, and load-bearing-land identification.

3.5. Effect of Dimple Overlap

Union area, overlap-corrected specific oil capacity, and working-pressure stiffness change systematically as texture pitch decreases at fixed forming force (Figure 9). For 400 N and $p = 250$ μm, the periodic footprint union reaches full saturation, i.e., it covers the entire unit cell; the overlap-corrected specific oil capacity is 6.52 μm, whereas isolated-dimple summation gives the upper bound 12.47 μm. The 47.7% reduction quantifies the importance of overlap at this design point. By contrast, the corrections for the $(200\ \text{N}, 350\ \mu\text{m})$ and $(400\ \text{N}, 500\ \mu\text{m})$ high-coverage design points are below 0.1% in both cases because the periodic cavities overlap only in shallow rim regions. Their relative oil-capacity ordering is unchanged by the periodic-union calculation. As the texture pitch decreases, the periodic footprint union expands, the remaining load-bearing land decreases, and the working-pressure stiffness consequently falls. The extrapolated trend toward $K_{work} \to 0$ indicates the loss of load-bearing land at full overlap and lies outside the computed range. At

$p \leq 200$ µm, the remaining land fraction falls outside the screening index's validity range, so a full contact calculation is required.

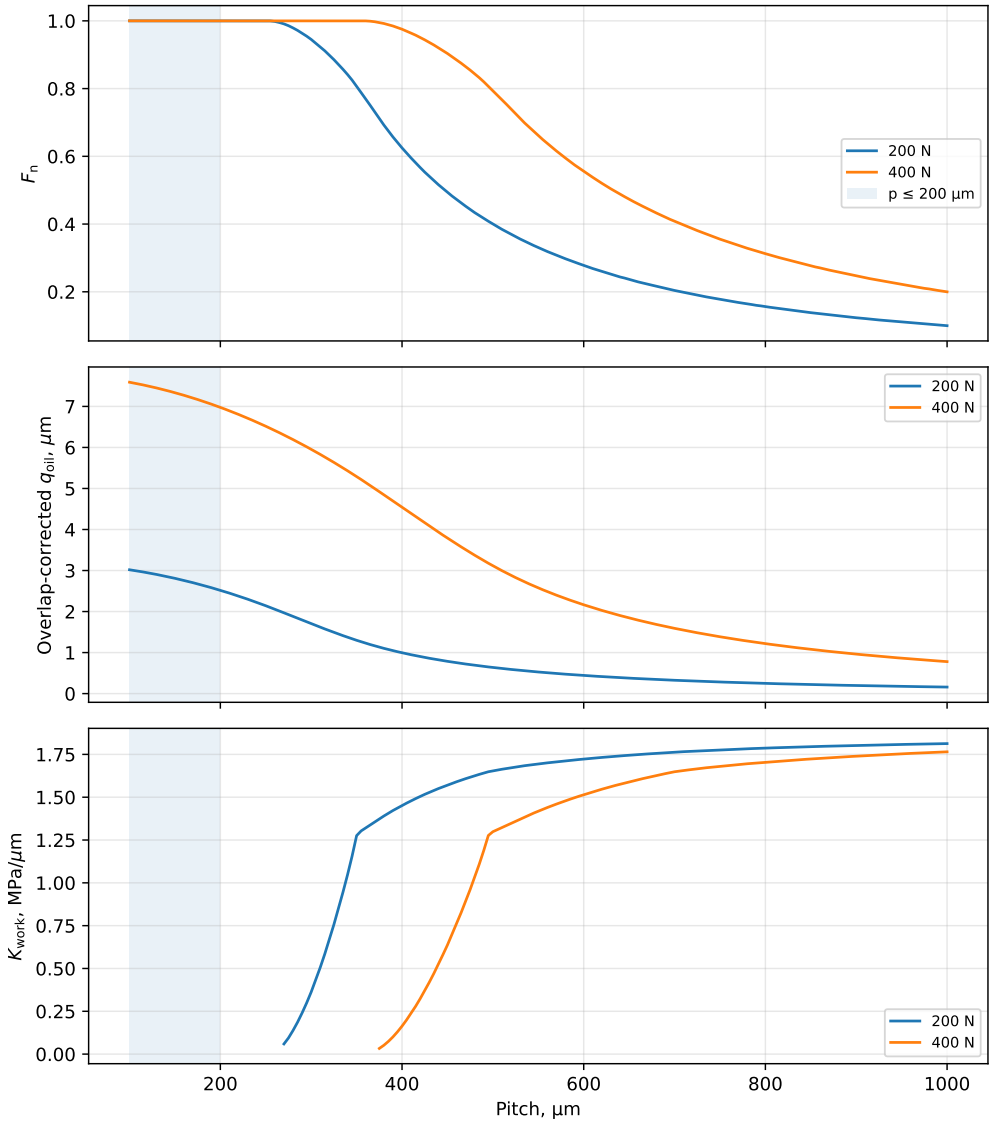


Figure 9. Effect of texture-pitch reduction at fixed burnishing forces of 200 and 400 N: union area fraction, overlap-corrected specific oil capacity, and interpolated working-pressure stiffness. The shaded band highlights the strongly overlapped $p \leq 200$ µm region; screening-index applicability is determined pointwise by $F_n \leq 0.20$, not by pitch alone.

3.6. Adaptive Stiffness Maps for a Soft Guideway

The soft-guideway design task is formulated as a multi-objective selection problem: choose a burnishing force F_N and a texture pitch p to (i) minimize the idle stiffness K_{low} at $q = 0.10$ MPa, (ii) maximize the working stiffness K_{work} at $q = 1.00$ MPa, and (iii) maintain the dimple area fraction $F_n < 1$ and a positive land fraction. Specific oil capacity q_{oil} is used as a secondary criterion for candidates with identical stiffness metrics. The prescribed stiffness windows define the feasible region, and the trade-off between the two objectives is evaluated by non-dominated sorting of the discrete force–pitch design points. Figure 10 shows the selection workflow.

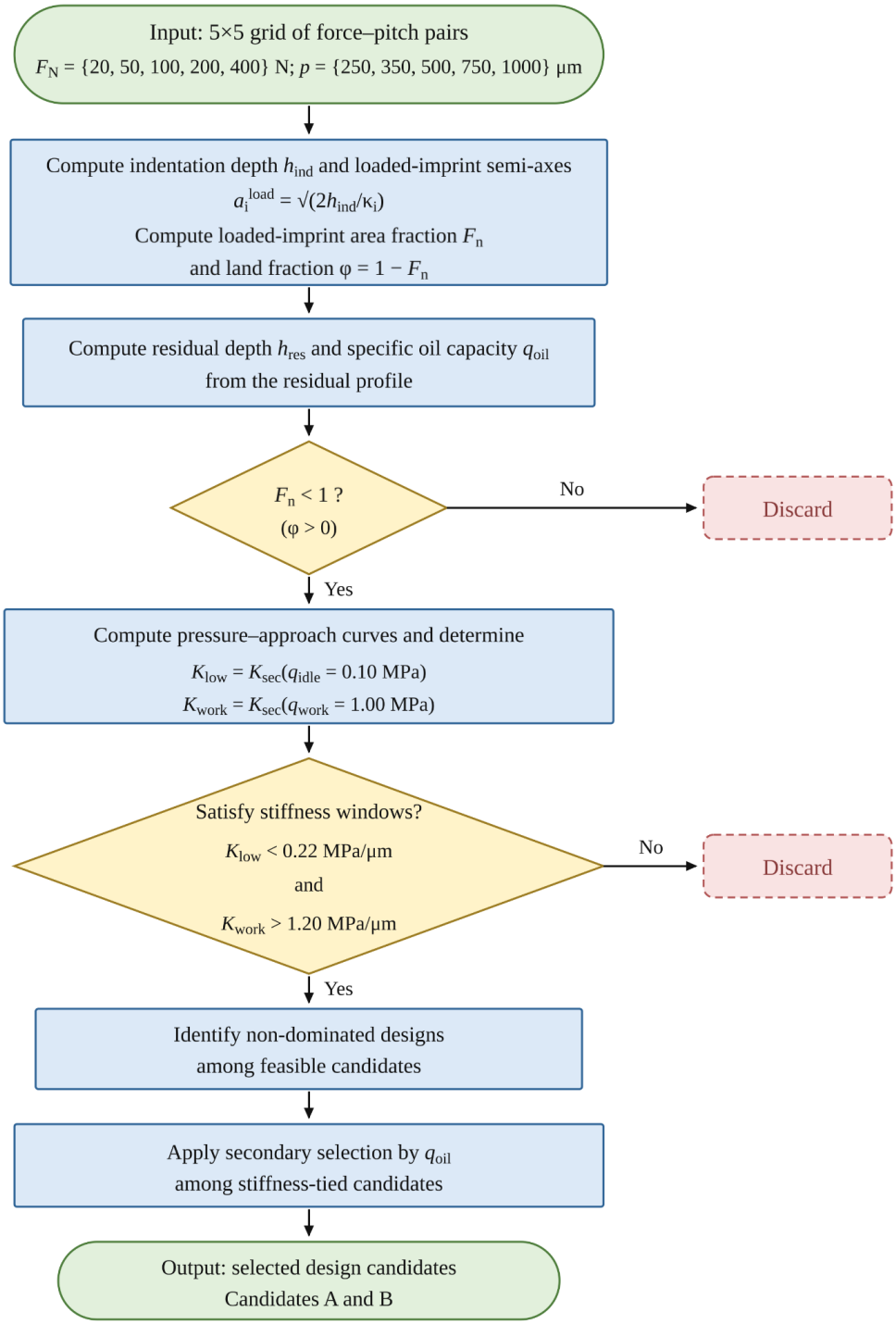


Figure 10. Flowchart for evaluating force–pitch design points using the area constraint, pressure–approach curves, stiffness thresholds, non-dominated sorting, and specific oil capacity.

The soft-guideway design case uses the force–pitch grid $F_N = \{20, 50, 100, 200, 400\}$ N and $p = \{250, 350, 500, 750, 1000\}$ µm. The substrate and load-bearing-land inputs were set to $E = 210$ GPa, $\nu = 0.30$, $H_{eff} = 2$ GPa (the illustrative baseline; see Section 3.7), $R_a = 0.20$ µm, and $R_{sm} = 0.50$ mm. The resulting idle- and working-pressure stiffness maps are given in Figure 11.

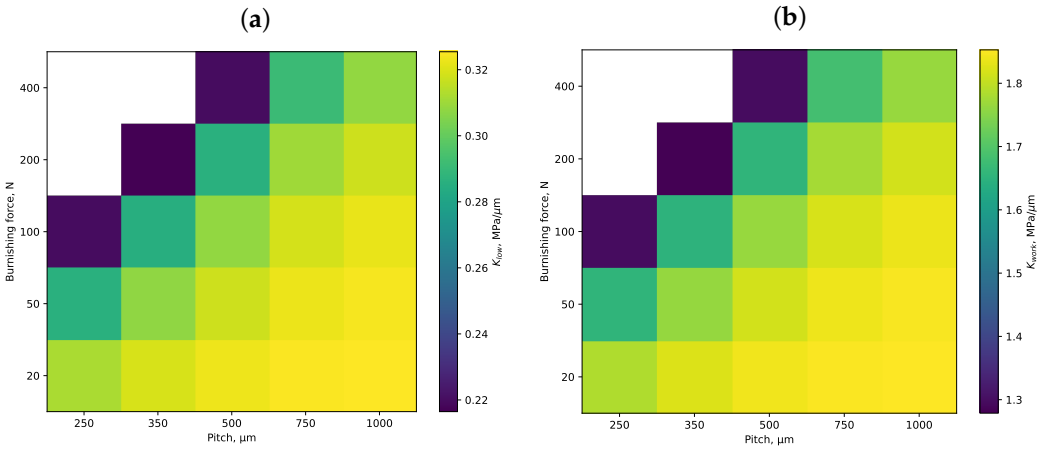


Figure 11. Force–pitch maps of secant stiffness: (**a**) idle pressure $q = 0.10$ MPa and (**b**) working pressure $q = 1.00$ MPa.

The nonlinearity ratio and the feasible region inherit the same land-fraction dependence (Figure 12).

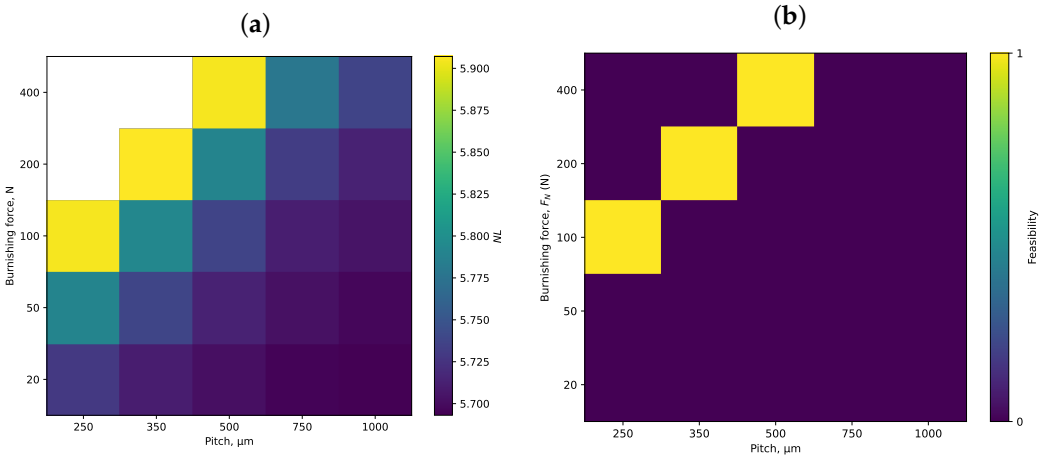


Figure 12. Force–pitch design maps: (**a**) nonlinearity ratio $NL = K_{\text{work}}/K_{\text{low}}$ and (**b**) feasible region of the prescribed stiffness-window case.

The design problem has two stiffness objectives: low K_{low} and high K_{work}, with NL used as a derived measure. Because only 25 discrete force–pitch combinations are evaluated, the analysis identifies non-dominated points. Of the 25 design points, three satisfy the stiffness windows and positive-land constraint, and all three are non-dominated. Two of the three feasible points—$(100\ \text{N}, 250\ \mu\text{m})$ and $(400\ \text{N}, 500\ \mu\text{m})$—share the same idle- and working-pressure stiffnesses. Of these two stiffness-tied points, $(100\ \text{N}, 250\ \mu\text{m})$ is removed because it has the lower specific oil capacity (0.436 µm), leaving $(400\ \text{N}, 500\ \mu\text{m})$ as Candidate B. The third feasible point, which has a distinct stiffness pair, is Candidate A (Figure 13).

The non-dominated set occupies a narrow, steep region of the K_{low}–K_{work} plane because both stiffness metrics are governed primarily by land fraction. Increasing texture coverage lowers K_{low} but also lowers absolute K_{work}; useful design points therefore lie close to the imposed K_{work} floor. Forming force provides a second design variable because it increases residual depth and specific oil capacity without uniquely determining F_{n}: design points with the same stiffness pair can store very different volumes. Table 7 reports the two candidates selected after comparison of specific oil capacity. Candidate A gives the lowest idle stiffness, whereas Candidate B provides greater specific oil capacity at comparable idle- and working-pressure stiffnesses. The same area–stiffness trade-off is shown in Figure 14.

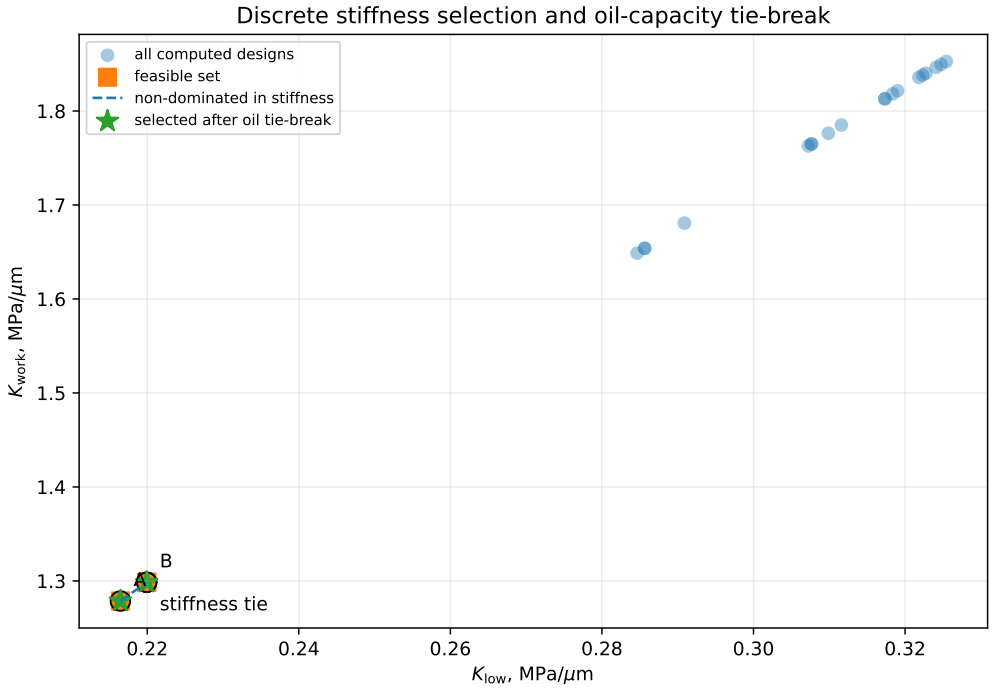


Figure 13. Discrete selection in the K_{low}–K_{work} objective plane. All 25 force–pitch design points are shown; the three feasible points are non-dominated in stiffness, and stars identify the two candidates selected after comparison of specific oil capacity.

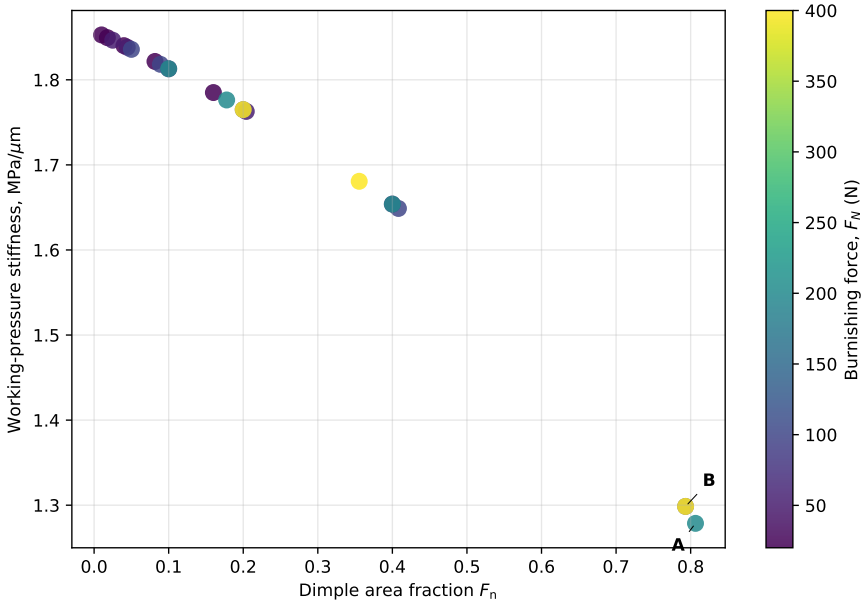


Figure 14. Design candidates in the (F_n, K_{work}) plane. The two selected candidates are annotated.

Table 7. Soft-guideway candidates selected after non-dominated sorting and comparison of specific oil capacity. Stiffness values are rounded for presentation; feasibility and selection use unrounded values.

Design	F_N (N)	p (μm)	K_{low}	K_{work}	NL	q_{oil} (μm)	Selection Basis
A	200	350	0.217	1.28	5.91	1.30	lowest idle stiffness
B	400	500	0.220	1.30	5.90	3.12	higher oil capacity among tied candidates

The feasible set is conditional on the illustrative stiffness windows. A threshold sweep (Supplementary Section S4, Table S3) shows that the set is unchanged for the tested relaxations of either threshold and for the tested 5% increase in the working-stiffness floor, whereas tighter idle-stiffness limits remove all feasible points. The reported candidates therefore demonstrate the selection procedure rather than universal design optima.

Both selected candidates produce greater approach and lower secant stiffness than the nearly untextured reference over the full pressure range (Figure 15).

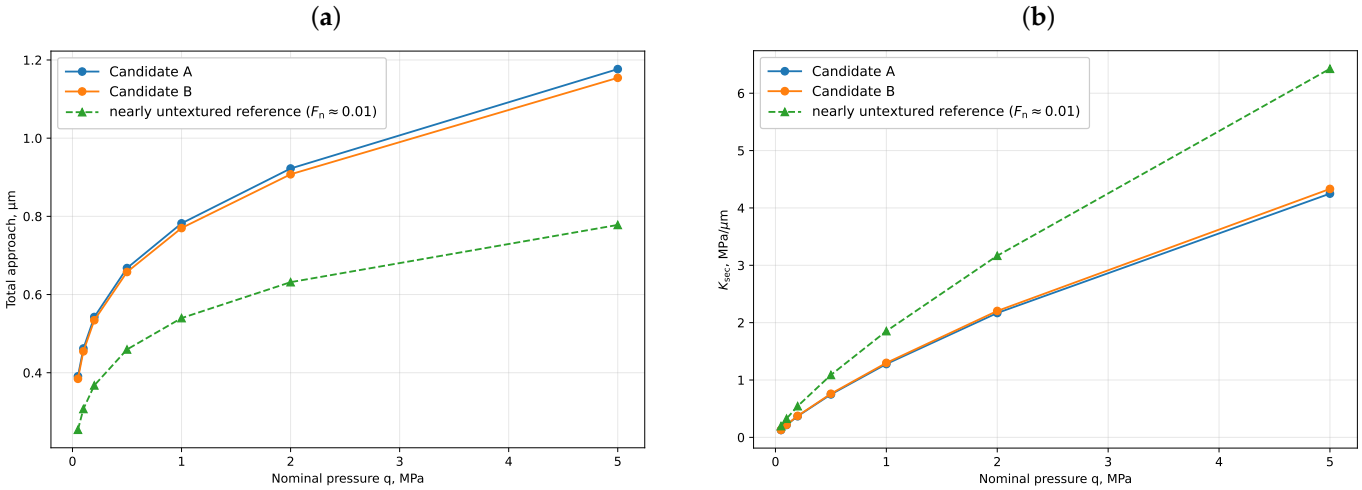


Figure 15. Pressure response of selected guideway candidates and the nearly untextured reference ($F_N = 20$ N, $p = 1000\,\mu$m): (**a**) pressure–approach curves and (**b**) secant stiffness curves $K_{sec}(q) = q/\delta(q)$.

For reference, Figure 15 also shows the response of a nearly untextured plateau with the same load-bearing-land roughness (the $F_N = 20$ N, $p = 1000\,\mu$m design point, $F_n \approx 0.01$, $h_{res} = 0$). Relative to this baseline, the regular microrelief lowers the secant stiffness at all pressures: for Candidate A the idle stiffness decreases by approximately 33% (from 0.325 to 0.217 MPa/μm) and the working stiffness by about 31% (from 1.85 to 1.28 MPa/μm); Candidate B differs from these values by less than 2%. The idle stiffness decreases more strongly than the working stiffness, producing a modest increase in the nonlinearity ratio from $NL = 5.70$ to 5.91 (approximately 3.7%).

Applying the curvature-based residual-profile approximation to the same 25 design points yields no point that satisfies both stiffness windows. The nominal maps use the periodic union of loaded-imprint footprints, whereas the sensitivity calculation rebuilds each footprint from h_{res} while retaining the same load-bearing-land pressure–approach law and selection windows. Table 8 and Figure 16 quantify the change: the smaller parabolic footprints leave more land, increasing both K_{low} and K_{work} but reducing NL slightly. The selected candidates are therefore sensitive to the curvature-based residual-profile approximation, and the loaded-imprint assumption should be checked against measured profiles before the manufacturing parameters are finalized.

Table 8. Selected-design metrics for the nominal loaded-imprint maps and the curvature-based residual-profile sensitivity calculation.

Design	Geometry	F_n	q_{oil}	K_{low}	K_{work}	NL
A	loaded imprint	0.807	1.30	0.217	1.28	5.91
A	curvature-based approximation	0.463	0.74	0.278	1.61	5.81
B	loaded imprint	0.793	3.12	0.220	1.30	5.90
B	curvature-based approximation	0.555	2.16	0.265	1.55	5.84

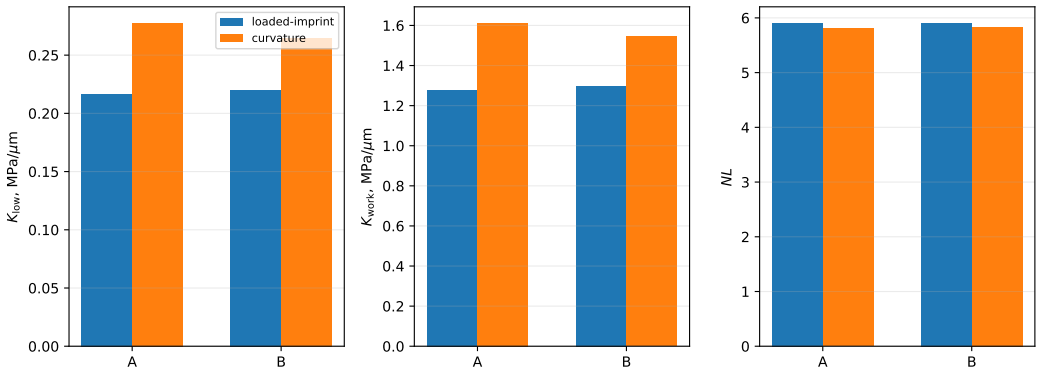


Figure 16. Candidate A/B stiffness metrics for the nominal loaded-imprint maps and the curvature-based residual-profile sensitivity calculation.

The area and volume of the curvature-based residual-profile approximation decrease in the same proportion for an isolated elliptic paraboloid because $V = Ah_{\mathrm{res}}/2$. After periodic clipping, however, footprint area controls the land fraction and hence both stiffnesses, whereas depth additionally controls the retained volume. This separates specific oil capacity from stiffness and explains why changing the residual-profile reconstruction has a larger effect on candidate feasibility than on NL.

3.7. Sensitivity to Material and Surface Parameters

The pressure–approach model was evaluated over a roughness and material grid to quantify sensitivity to load-bearing-land properties. The sweep uses the fixed reference texture $F_{\mathrm{n}} = 0.20$ ($\phi = 0.80$), $\delta_{\mathrm{reg}} = 0$, and $q_{\mathrm{land}} = q_{\mathrm{nom}}/0.80$. It comprised 50 parameter sets evaluated at six pressures (Figure 17). Thirty-nine sets satisfy $\chi_{\mathrm{GW}} \leq 0.30$ and use the elastic formulation; the remaining 11 fall outside the elastic screening range and require an elastic–plastic extension for quantitative use.

The sensitivity of the stiffness response to load-bearing-land variations was quantified with the reference-texture sweep of Figure 17. Within this sweep, increasing roughness from $R_{\mathrm{a}} = 0.20$ to 0.28 µm lowers the secant stiffness by 21% at the idle pressure and by 23% at the working pressure, while reducing the elastic modulus from 210 to 110 GPa lowers them by 16% and 14%, respectively (approximately 3–4% for each 10% change in elastic modulus). Both stiffness metrics of the selected candidates scale with these land-property factors to first order, whereas the ratio $NL = K_{\mathrm{work}}/K_{\mathrm{low}}$ changes by less than 3% over the examined range. The same trend applies to the selected design region in Figure 18: the deterministic dimple geometry is fixed by burnishing force and texture pitch, whereas the load-bearing land remains sensitive to elastic modulus and roughness descriptors. Absolute stiffness maps should therefore be paired with the measured roughness and elastic modulus of the finished land.

The effective mean indentation pressure shifts the feasible region of the design maps (Figure 19). The 1, 2, and 3 GPa values define illustrative sensitivity cases for the effective mean indentation pressure. From $A_{\mathrm{proj}} = F_{\mathrm{N}}/H_{\mathrm{eff}}$, preserving the same loaded-imprint area and land fraction requires, to first order, $F_{\mathrm{N}} \propto H_{\mathrm{eff}}$. The map therefore shifts toward lower force when H_{eff} decreases and toward higher force when it increases. Residual depth and specific oil capacity do not follow this linear scaling because $h_{\mathrm{res}} = h_{\mathrm{ind}} - h_{\mathrm{rec}}$ and the unloading term depends on the contact radius; this nonlinear recovery is most influential for shallow dimples. In the present 20–400 N grid, the 3 GPa feasible region lies above the computed force range.

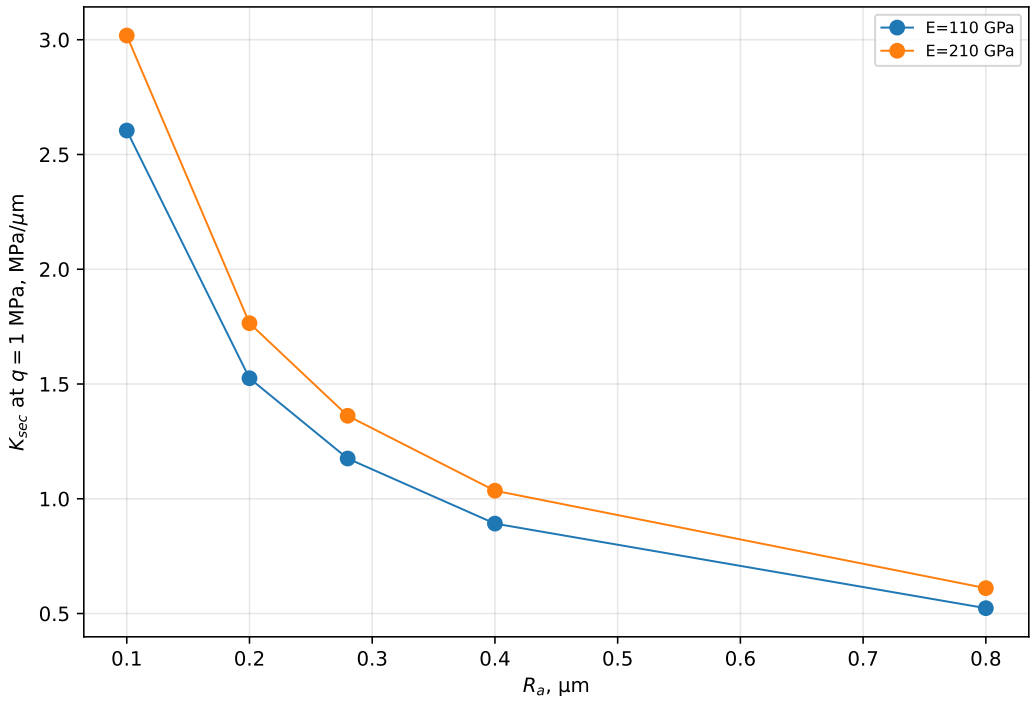


Figure 17. Sensitivity of the pressure–approach response at $q = 1$ MPa to load-bearing-land roughness and material inputs. The circles mark the evaluated R_a values at $R_{sm} = 0.50$ mm.

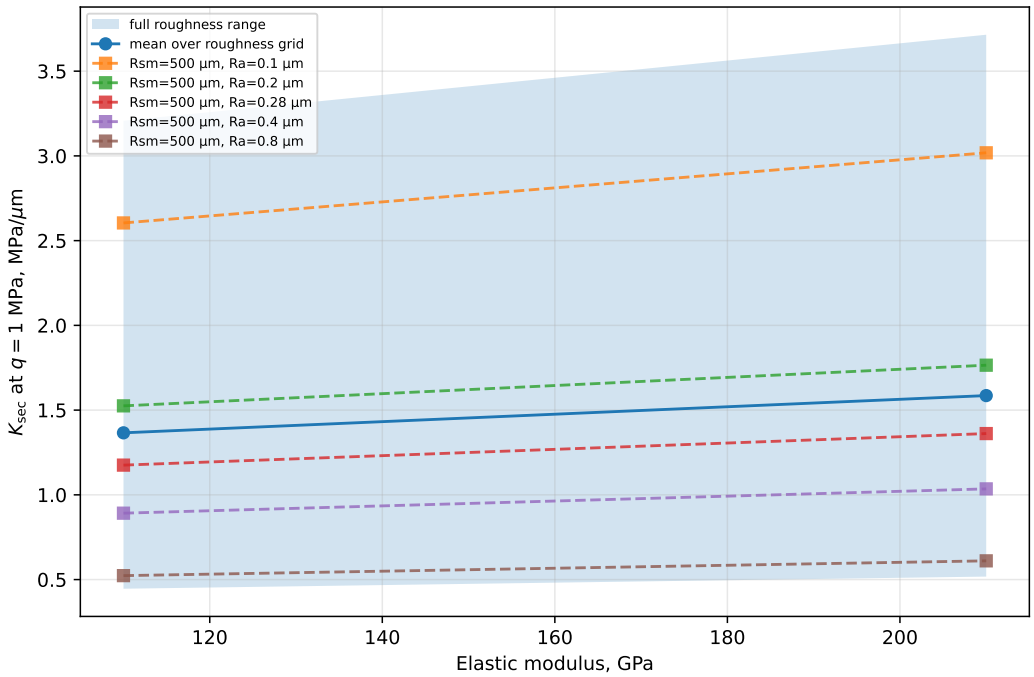


Figure 18. Land-roughness and material-modulus sensitivity at $q = 1$ MPa.

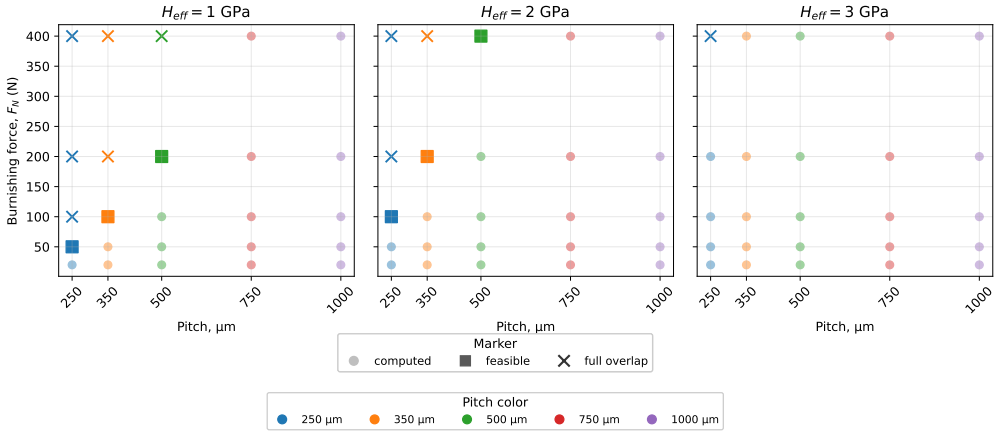


Figure 19. Numerical sensitivity of the force–pitch feasible region to the effective mean indentation pressure. Squares mark design points satisfying the illustrative stiffness-window criteria; crosses mark full-overlap points with insufficient land fraction.

4. Discussion

4.1. Physical Interpretation and Engineering Implications

Within the evaluated force–pitch range, the calculations show a trade-off between specific oil capacity and contact stiffness. Increasing F_N increases residual depth and oil capacity while the loaded-imprint union reduces the load-bearing land. Because isolated parabolic volume scales as $Ah_{res}/2$, design points with the same land fraction can have the same stiffness pair and markedly different q_{oil}. Periodic clipping is negligible for Candidates A and B but becomes decisive near full overlap.

The selected textures do not increase absolute stiffness relative to the nearly untextured reference. Instead, they redistribute pressure-dependent compliance by preferentially reducing idle-pressure stiffness, which produces a modest increase in NL from 5.70 to 5.91. The result supports the adopted definition of adaptive response as passive pressure dependence, without implying active control or absolute stiffness gain.

Residual-profile reconstruction is the largest geometric sensitivity examined in the present maps. Within the land-only stiffness closure, the loaded-imprint union gives lower stiffness because it leaves less land, whereas the curvature-based residual-profile approximation gives higher stiffness. These are alternative analytical geometries rather than universal physical bounds. Their different candidate sets quantify the consequence of profile uncertainty and identify residual profilometry as the relevant identification input before transferring the force–pitch map to a particular material and burnishing regime.

The framework combines established contact-mechanics elements: hardness as a mean indentation pressure, local nonconforming geometry and equivalent-punch unloading, Greenwood–Williamson rough-land contact, and the elastic half-space Green function used in spectral and FFT-BEM calculations [30,38,40–42]. The contribution is the common force → depth → geometry → stiffness chain, the separation of nominal map and spectral-reference roles, and the conditional selection procedure. The FFT-BEM benchmark and spectral comparison provide numerical verification and model-consistency evidence for their respective calculations; process-specific measurements are required to assess predictions for a particular workpiece and interface.

From a process-planning perspective, the framework reduces the number of force–pitch combinations that require higher-fidelity calculation or testing. Material-specific use requires force–depth or residual-profile data to identify H_{eff} and λ, together with a measured or independently calibrated pressure–approach relation for the load-bearing

land. The resulting maps can then prioritize candidate settings for application-specific verification.

4.2. Limitations and Scope

The present model is limited to metallic substrates, particularly steel, under quasi-static forming and room-temperature service conditions. Viscoelastic memory effects are relevant to polymers, viscoelastic coatings, and elevated-temperature processes; those cases require hereditary, fractional, or viscoplastic constitutive relations and are outside the present elastic–plastic closure. More detailed deterministic–microlevel (multiscale) formulations can be used when texture compliance, micro-roughness plasticity, and topology coupling must be resolved explicitly [44].

At the forming stage, friction, strain hardening, pile-up, residual-stress gradients, and initial topography can materially change the force–depth relation and the post-unloading profile [17–20]. They are not resolved as separate fields here. Measured force–depth and residual-profile data would be required to identify H_{eff} and λ for a specific material–process pair. After such identification, these parameters may represent part of the net effect of material-specific recovery and forming history on the global force–area and unloading relations; they do not reproduce local frictional flow, pile-up morphology, residual-stress fields, or the detailed residual geometry, and they do not replace a friction-resolving forming model. At the service stage, lubrication, wear evolution, and thermal history require separate tribological or time-dependent models and are not represented by these two identification parameters. Measured force–depth or residual-profile data are required for the forming module, while pressure–approach or dynamic-compliance measurements are required for the land-stiffness module. These checks establish the numerical and analytical accuracy of the stated formulation; transfer to a specific material–process pair remains controlled by residual-profile, material-response, and load-bearing-land identification.

The framework remains modular: measured profilometry can replace the analytical cavity, a measured pressure–approach curve can replace the Greenwood–Williamson land law, and the full spectral or unilateral periodic calculation can replace the screening index without changing the overall candidate-selection procedure.

5. Conclusions

A coupled force–depth–stiffness framework was developed for regular dimples produced by rotary ball burnishing on an external cylindrical surface. It links forming force and texture pitch to loaded-imprint geometry, residual oil-retention geometry, and pressure-dependent land stiffness, providing a reproducible route from process variables to preliminary stiffness-map selection.

The calculations show that elastic recovery separates the post-unloading profile from the loaded imprint used in the nominal land-stiffness maps. The curvature-based recalculation changes the feasible set, identifying measured residual geometry as the most informative input for material-specific map transfer. Periodic-union clipping is negligible for the two selected candidates but becomes essential as the footprints approach full overlap.

Within $F_{\mathrm{n}} \leq 0.20$, the low-fidelity index preserves the spectral ordering of the evaluated design points. The observed pointwise differences support its use for preliminary ranking, with tied and boundary-sensitive cases passed to the spectral calculation. Under the illustrative stiffness windows, the discrete map yields two selected force–pitch candidates after non-dominated sorting and secondary selection by specific oil capacity.

The selected textures reduce idle-pressure stiffness slightly more than working-pressure stiffness, producing a modest increase in NL from 5.70 to 5.91. Across the examined land-roughness and elastic-modulus ranges, NL changes by less than 3%, whereas abso-

lute stiffness remains more sensitive to land properties. Once H_{eff}, λ, residual geometry, and the land pressure–approach response are identified for a material–process pair, the same mapping and selection procedure can be reused for application-specific design. The framework therefore supports reproducible preliminary screening; quantitative application to a specific material–process pair requires identification and validation of the forming and land-contact parameters.

Supplementary Materials: The following supporting information can be downloaded at: https://www.mdpi.com/article/10.3390/technologies14080514/s1, Supplementary Materials report the numerical settings, convergence checks, complete force–pitch grids, and stiffness-threshold sensitivity analysis. Figure S1: Dimple area fraction and specific oil capacity from the spherical-unloading approximation; Figure S2: Material and load-bearing-land roughness sensitivity of secant stiffness at $q = 1$ MPa; Table S1: Nominal loaded-imprint force–pitch grid with feasibility, non-dominance, and final-selection indicators; Table S2: Curvature-based residual-profile force–pitch grid; Table S3: Threshold sensitivity of the feasible and selected sets.

Author Contributions: Conceptualization, methodology, formal analysis, and writing—original draft preparation: K.A.B.; numerical verification, data curation, and writing—review and editing: I.S.N.; supervision and writing—review and editing: A.V.Z. All authors have read and agreed to the published version of the manuscript.

Funding: This research received no external funding.

Data Availability Statement: The datasets and source code generated during the current study are available from the corresponding author upon reasonable request.

Conflicts of Interest: The authors declare no conflicts of interest.

Abbreviations

RMR	Regular microrelief
FFT-BEM	Fast Fourier transform boundary-element method
NL	Nonlinearity ratio, $K_{\text{work}}/K_{\text{low}}$

References

1. Wang, L.; Liu, H.; Zhang, J.; Zhao, W. Analysis and modeling for flexible joint interfaces under micro and macro scale. *Precis. Eng.* **2013**, *37*, 817–824. [CrossRef]
2. Li, L.; Wang, J.; Pei, X.; Chu, W.; Cai, A. A new method for modeling mechanical joint surface contact stiffness. *J. Mech. Eng.* **2020**, *56*, 162–169. [CrossRef]
3. Zhang, C.; Yu, W.; Yin, L.; Zeng, Q.; Chen, Z.; Shao, Y. Modeling of normal contact stiffness for surface with machining textures and analysis of its influencing factors. *Int. J. Solids Struct.* **2023**, *262–263*, 112042. [CrossRef]
4. Saito, T. Development of Machine Tool's Guideways—Dynamically Pressurized, Statically Pressurized and Partially Floated Guideways. *JTEKT Eng. J. Engl. Ed.* **2006**, *1001E*, 57–64.
5. Zha, J.; Cheng, K.; Xue, F.; Wu, D.; Liu, X. Hydrostatic guideways for precision machines: The state-of-the-art and future perspectives. *Tribol. Int.* **2024**, *200*, 110060. [CrossRef]
6. Oh, J.-S.; Sohn, J.W.; Choi, S.-B. Applications of Magnetorheological Fluid Actuator to Multi-DOF Systems: State-of-the-Art from 2015 to 2021. *Actuators* **2022**, *11*, 44. [CrossRef]
7. He, Y.; Fu, Y.; Wang, H.; Yang, J. Inhibiting mechanism of micro dimples on the stick-slip of sliding guideway: Combined numerical analysis with tribological tests. *Tribol. Int.* **2021**, *162*, 107144. [CrossRef]
8. Yue, H.; Deng, J.; Ge, D.; Li, X.; Zhang, Y. Effect of surface texturing on tribological performance of sliding guideway under boundary lubrication. *J. Manuf. Process.* **2019**, *47*, 172–182. [CrossRef]
9. Shneyder, Y.G. *Operational Properties of Parts with Regular Microrelief*, 2nd ed.; Mashinostroenie: Leningrad, USSR , 1982. (In Russian)
10. Dzyura, V.; Maruschak, P. Optimizing the formation of hydraulic cylinder surfaces, taking into account their microrelief topography analyzed during different operations. *Machines* **2021**, *9*, 116. [CrossRef]

11. Dzyura, V.; Maruschak, P.; Slavov, S.; Dimitrov, D.; Semehen, V.; Markov, O. Evaluating some functional properties of surfaces with partially regular microreliefs formed by ball-burnishing. *Machines* **2023**, *11*, 633. [CrossRef]
12. Zhou, Z.-Y.; Zheng, Q.-Y.; Ding, C.; Yan, J.-Y.; Piao, Z.-Y. A review of the development of surface burnishing process technique based on bibliometric analysis and visualization. *Int. J. Adv. Manuf. Technol.* **2021**, *115*, 1955–1999. [CrossRef]
13. Liu, Z.; Dai, Q.; Deng, J.; Zhang, Y.; Ji, V. Analytical modeling and experimental verification of surface roughness in the ultrasonic-assisted ball burnishing of shaft targets. *Int. J. Adv. Manuf. Technol.* **2020**, *107*, 3593–3613. [CrossRef]
14. Nagit, G.; Dodun, O.; Slatineanu, L.; Ripanu, M.; Mihalache, A.; Hrituc, A. Influence of some process input factors on the main dimensions of the grooves generated during the ball vibroburnishing. *IOP Conf. Ser. Mater. Sci. Eng.* **2020**, *968*, 012007. [CrossRef]
15. Nagit, G.; Slatineanu, L.; Dodun, O.; Ripanu, M.I.; Mihalache, A.M. Surface layer microhardness and roughness after applying a vibroburnishing process. *J. Mater. Res. Technol.* **2019**, *8*, 4333–4346. [CrossRef]
16. Gurey, V.; Maruschak, P.; Hurey, I.; Dzyura, V.; Hurey, T.; Wojtowicz, W. Dynamic analysis of the thermo-deformation treatment process of flat surfaces of machine parts. *J. Manuf. Mater. Process.* **2023**, *7*, 101. [CrossRef]
17. Becerra-Becerra, E.; Aguilera Ojeda, C.O.; Saldaña-Robles, A.; Reveles-Arredondo, J.F.; Barco-Burgos, J.; Vidal-Lesso, A. A review of numerical simulation of ball burnishing process. *Finite Elem. Anal. Des.* **2023**, *218*, 103926. [CrossRef]
18. Torres, A.; Amini, C.; Cuadrado, N.; Travieso-Rodriguez, J.A.; Llumà, J.; Vilaseca, M. Experimental validation of ball burnishing numerical simulation on ball-end milled martensitic stainless-steel considering friction and the initial surface topography. *J. Mater. Res. Technol.* **2023**, *22*, 3352–3361. [CrossRef]
19. Teimouri, R.; Grabowski, M.; Bogucki, R.; Ślusarczyk, L.; Skoczypiec, S. Modeling of strengthening mechanisms of surface layers in burnishing process. *Mater. Des.* **2022**, *223*, 111114. [CrossRef]
20. Charfeddine, Y.; Youssef, S.; Sghaier, S.; Sghaier, J.; Hamdi, H. Study of the simultaneous grinding/ball-burnishing of AISI 4140 based on finite element simulations and experiments. *Int. J. Mech. Sci.* **2021**, *192*, 106097. [CrossRef]
21. Swirad, S.; Gradzik, A.; Ochał, K.; Pawlus, P. Effects of the surface layer of steel samples after ball burnishing on friction and wear in dry reciprocating sliding. *Sci. Rep.* **2023**, *13*, 11088. [CrossRef] [PubMed]
22. Skoczylas, A.; Zaleski, K. Selected properties of the surface layer of C45 steel parts subjected to laser cutting and ball burnishing. *Materials* **2020**, *13*, 3429. [CrossRef] [PubMed]
23. Mao, Y.; Zhang, Y.; Zheng, J.; Li, L.; Huang, Y.; Shi, S.; Wang, L.; Pei, J.; Li, Z. A study on micro-pit texture parameter optimization and its tribological properties. *Machines* **2024**, *12*, 475. [CrossRef]
24. Zhang, Q.X.; Mo, J.L.; Xiang, Z.Y.; Wang, Q.; Yu, Z.; Zhai, C.Z.; Zhu, S. Effect of surface micro-grooved textures in suppressing stick-slip vibration in high-speed train brake systems. *Tribol. Int.* **2023**, *189*, 108946. [CrossRef]
25. Zhang, Q.; Liu, Q.-A.; Mo, J.; Xiang, Z.; Wang, Q.; Zhai, C.; Zhu, S. Analysis of contact characteristics and dynamic response of joint interface with surface micro-grooved texture based on fractal theory. *Mech. Syst. Signal Process.* **2024**, *218*, 111553. [CrossRef]
26. Hong, M.S.; Ehmann, K.F. Generation of engineered surfaces by the surface-shaping system. *Int. J. Mach. Tools Manuf.* **1995**, *35*, 1269–1290. [CrossRef]
27. Greco, A.; Raphaelson, S.; Ehmann, K.; Wang, Q.J.; Lin, C. Surface texturing of tribological interfaces using the vibromechanical texturing method. *J. Manuf. Sci. Eng.* **2009**, *131*, 061005. [CrossRef]
28. Bashmur, K.A.; Zagulyaev, A.V. Influence of Surface Relief on Dynamic Characteristics of the Rotor–Bearing System of a Centrifugal Pump. *MIAB Min. Inf. Anal. Bull.* **2026**, *5*, 20–38. Available online: https://giab-online.ru/files/Data/2026/5/05_2026_20-38.pdf (accessed on 16 August 2026). (In Russian). [CrossRef]
29. Bashmur, K.A.; Morin, A.S.; Zagulyaev, A.V.; Nebylitsyn, M.V. Improving the tribological characteristics of hydraulic prop support equipment of powered roof support with nature-inspired technologies. *Sustain. Dev. Mt. Territ.* **2025**, *17*, 1875–1886. (In Russian) [CrossRef]
30. Greenwood, J.A.; Williamson, J.B.P. Contact of nominally flat surfaces. *Proc. R. Soc. Lond. A* **1966**, *295*, 300–319. [CrossRef]
31. Kogut, L.; Etsion, I. Elastic-plastic contact analysis of a sphere and a rigid flat. *J. Appl. Mech.* **2002**, *69*, 657–662. [CrossRef]
32. Bhushan, B. *Introduction to Tribology*, 2nd ed.; Wiley: Hoboken, NJ, USA, 2013.
33. Yu, X.; Sun, Y.; Zhao, D.; Wu, S. A revised contact stiffness model of rough curved surfaces based on the length scale. *Tribol. Int.* **2021**, *164*, 107206. [CrossRef]
34. Zhai, C.; Hanaor, D.; Proust, G.; Gan, Y. Contact stiffness of multiscale surfaces by truncation analysis. *Int. J. Mech. Sci.* **2017**, *131–132*, 305–316. [CrossRef]
35. Yang, T.; Peng, H.; Wang, G.; Tang, X.; Zheng, Y. A unified scale-coupling homogenized contact model for elasto-plastic rough surfaces with textures. *Tribol. Int.* **2025**, *212*, 110995. [CrossRef]
36. Goryacheva, I.G.; Tsukanov, I.Y. Analysis of elastic normal contact of surfaces with regular microgeometry based on the localization principle. *Front. Mech. Eng.* **2020**, *6*, 45. [CrossRef]
37. Tsukanov, I.Y. An extended asymptotic analysis for elastic contact of three-dimensional wavy surfaces. *Tribol. Lett.* **2019**, *67*, 107. [CrossRef]

38. Mueser, M.H.; Dapp, W.B.; Bugnicourt, R.; Sainsot, P.; Lesaffre, N.; Lubrecht, T.A.; Persson, B.N.J.; Harris, K.; Bennett, A.; Schulze, K. ; et al. Meeting the contact-mechanics challenge. *Tribol. Lett.* **2017**, *65*, 118. [CrossRef]
39. Yastrebov, V.A.; Anciaux, G.; Molinari, J.-F. From infinitesimal to full contact between rough surfaces: Evolution of the contact area. *Int. J. Solids Struct.* **2015**, *52*, 83–102. [CrossRef]
40. Johnson, K.L. *Contact Mechanics*; Cambridge University Press: Cambridge, UK, 1985.
41. Tabor, D. *The Hardness of Metals*; Oxford University Press: Oxford, UK, 1951.
42. Oliver, W.C.; Pharr, G.M. An improved technique for determining hardness and elastic modulus using load and displacement sensing indentation experiments. *J. Mater. Res.* **1992**, *7*, 1564–1583. [CrossRef]
43. Davoodi, F.; Guglielmi, P.; Palumbo, G.; Carbone, G. Experimental evaluation of 100Cr6 steel microindented surfaces under lubricated nonconformal point contacts. *Adv. Eng. Mater.* **2026**, *28* , e202500646. [CrossRef]
44. Bashmur, K.A.; Zagulyaev, A.V. Hybrid deterministic–microlevel model of normal contact stiffness for textured surfaces. *Lubricants* **2026**, *14*, 289. [CrossRef]

Disclaimer/Publisher's Note: The statements, opinions and data contained in all publications are solely those of the individual author(s) and contributor(s) and not of MDPI and/or the editor(s). MDPI and/or the editor(s) disclaim responsibility for any injury to people or property resulting from any ideas, methods, instructions or products referred to in the content.